Lawrence Berkeley National Laboratory
LBL Publications

Title

Calibration, modeling, parameterization, and verification of the instrument transfer function of an interferometric microscope

Permalink
https://escholarship.org/uc/item/4rm008db

Authors
Takacs, PZ
Rochester, S
Lacey, I
et al.

Publication Date
2022-10-03

DOI
10.1117/12.2633116

Peer reviewed

eScholarship.org Powered by the California Digital Library
University of California

Calibration, modeling, parameterization, and verification of the Instrument Transfer Function of an interferometric microscope

P. Z. Takacs*[1], S. Rochester[2], I. Lacey[3], K. Munechika[4], and V. V. Yashchuk[3]
[1]Surface Metrology Solutions LLC, 19 S 1st St, Unit B901, Minneapolis, MN 55401 USA; [2]Rochester Scientific, LLC, 2041 Tapscott Avenue, El Cerrito, CA 94530, USA; [3]Advanced Light Source, LBNL, 1 Cyclotron Road, Berkeley, CA 94720, USA; [4]HighRI Optics, Inc., 5401 Broadway Terr, St. 304, Oakland, CA 94618, USA

ABSTRACT

Interferometric microscopes are used to measure surface roughness, from which the computed power spectral density function can be used to extract bandwidth-limited values of the various surface properties, such as root-mean-square (rms) height and slope errors. Measurements with a microscope equipped with different objectives that have an overlapping spatial frequency range usually give different rms results over the common frequency bandwidth. This is a result of different instrument transfer functions (ITFs) that attenuate spatial frequencies by different amounts over the overlapping range. We report on the use of binary pseudo-random array (BPRA) standards to characterize the ITF of an interferometric microscope with the various objectives. We use a simple model of a 1D binary Results show that the spectrum for an undersampled array is a cosine function, rather than a straight line, constant white noise spectrum. We have an analytical model of the ITF that includes the effects of an obscured aperture and defocus, in addition to the usual parameters of numerical aperture, wavelength, and sampling period. In addition, the model includes the effect of aliasing of spatial frequency components beyond the Nyquist back into the sub-Nyquist region. We compare the model PSD predictions to the measurements performed with different objectives. Departures of the measured PSDs from the model predictions indicate that there are higher-order ITF corrections yet to be identified and included in the model.

Keywords: Instrument transfer function, metrology, standard calibration artifact, binary pseudorandom array, power spectral density, Mirau interference objective.

1. INTRODUCTION

Interferometric microscopes are useful tools for measuring the surface roughness properties of precision optical components, such as mirrors used to reflect x-rays in synchrotron radiation (SR) beam lines.[1-3] The most useful property for assessing mirror surface quality for SR applications is the power spectral density (PSD) function of the surface roughness. Church and collaborators extended the theoretical work on optical scattering from smooth surfaces of Rice[4], and Beckmann and Spizzichino[5] to predict the scattering of x-rays from polished and diamond-turned surfaces[6-10]. The scattering theory hinges on the knowledge of the surface PSD function, which, in turn, depends on the measurement of the surface topography. At the time these theories were formulated, measurement of surface roughness to the level required for predicting optical scattering was limited to mechanical stylus instruments[11]. Surface roughness parameters over a limited spatial frequency range were derived from total integrated scatter measurements.[12] The development of the interferometric microscope in the late '70s and early '80s revolutionized the metrology of optical surfaces, as it was a non-contact method that minimized the risk of damage to delicate coated optics.[13-16] Church introduced the concept of bandwidth-limited statistics to the analysis of surface roughness in the spatial frequency domain.[9, 10, 17, 18] When the first surface profilers based on interferometric microscopes were used to measure surface properties, it was recognized early on that the spatial frequency response of the system, in terms of the instrument transfer function (ITF), needed to be taken into account in order to restore the attenuation of high frequencies by the microscope numerical aperture and the pixel sampling period.[18] These early works used a linearized version of the ITF based on the microscope objective numerical aperture (NA). More demanding applications today require more precise knowledge of the instrument transfer function.

*takacs.surfmetsoln@gmail.com; phone +1 631.833.0620

Various methods have been developed for calibrating the ITF of optical profilers, but they all have limitations. [3, 19, 20] de Groot provides a comprehensive analysis of the workings of interference-based microscope profilers. What is needed is a convenient way to calibrate the response of the instrument over the desired spatial frequency bandwidth. The ideal calibration artifact should be reproducible and have a known frequency spectrum over the profiler's bandwidth, so that departures from the nominal spectrum indicate the system ITF. This statement is strictly true only for linear systems. The interferometric microscope is an inherently non-linear system, so we must take care to address non-linear effects in our application of the calibration artifact to the measurement. Yashchuk and collaborators,[21-25] have developed a family of 1D binary pseudo-random grating (BPRG) and 2D binary pseudo-random array (BPRA) artifacts that have been shown to be useful for characterizing surface topography measuring instruments. This paper will discuss some of the issues involved in applying BPRAs to the characterization of interference microscope-based surface profilometers.

2. BPRG PSD SIMULATIONS

The mathematical parameters and technology involved in the development of 1D BPRGs and 2D BPRAs are discussed in a number of references and will not be reproduced here.[26-28] There are a few different types of BPRAs that have been produced as calibration artifacts for various metrology instruments.[29-31] Here we will be concerned with modeling the behavior of the Highly Randomized BPRA (HR BPRA), which is a more randomized version of the earlier pattern based on a uniformly redundant array (URA).[32] These patterns are lithographically produced on polished Si substrates and consist of an array of uniform height features with different minimum feature sizes (ground rules, grRule). A map of the current version of the artifact is shown in Fig. 1 along with a chart listing the details of each pattern.

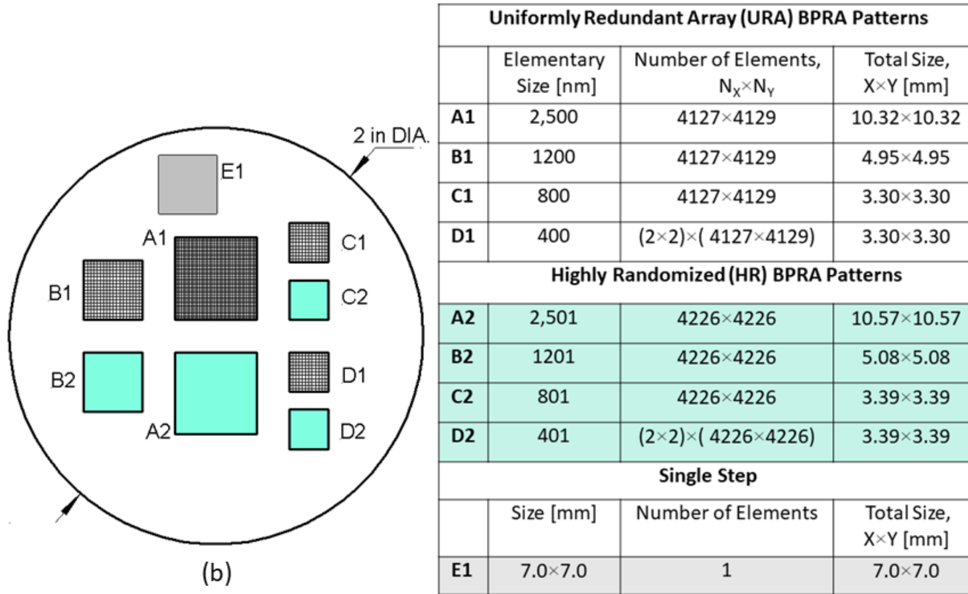

Uniformly Redundant Array (URA) BPRA Patterns			
	Elementary Size [nm]	Number of Elements, $N_X \times N_Y$	Total Size, X×Y [mm]
A1	2,500	4127×4129	10.32×10.32
B1	1200	4127×4129	4.95×4.95
C1	800	4127×4129	3.30×3.30
D1	400	(2×2)×(4127×4129)	3.30×3.30
Highly Randomized (HR) BPRA Patterns			
A2	2,501	4226×4226	10.57×10.57
B2	1201	4226×4226	5.08×5.08
C2	801	4226×4226	3.39×3.39
D2	401	(2×2)×(4226×4226)	3.39×3.39
Single Step			
	Size [mm]	Number of Elements	Total Size, X×Y [mm]
E1	7.0×7.0	1	7.0×7.0

Figure 1 - Current version of the BPRA on a 2" dia. substrate, containing both URA and HR patterns. The nominal height of the BPRA features used in this study is 60nm.

Table 1 shows all the relevant sampling parameters for the 4 objective lenses with 3 zoom settings for the Zygo NewView-9000™ in the Advanced Light Source (ALS) X-Ray Optics Laboratory (XROL). This microscope has a 1200 x 1600 pixel camera with 8.68µm square pixels but the current measurements are recorded on a 1000x1000 pixel subset grid. The nominal wavelength of the illumination system is 550nm. Each objective has a numerical aperture (NA) that, along with the wavelength, determines the maximum spatial frequency transmitted by the system, f_{NA}. This cutoff frequency is given by $f_{NA} = 2NA/\lambda$. The effective magnification, given by the product of the objective magnification and the zoom lens parameter, determines the size of the camera pixels projected onto the BPRA object. The field of view for each magnification is the overall apparent size of the camera area, indicated by the "Total trace length" column. The inverse of this parameter determines the fundamental frequency in the PSD. We use the one-sided periodogram estimator as our PSD function.[33] The frequency values in the PSD are integer multiples of the fundamental with the highest frequency given by the sampling Nyqist frequency (fNy), which is the inverse of twice the projected pixel pitch. If the

object contains features with power at frequencies greater than fNy, that power can be aliased back into the sub-Nyquist region and contaminates the observed spectrum This is an example of a non-linear process involved in the measurement. If, however, the objective lens cutoff is before the Nyquist frequency, the lens acts as a low-pass filter and prevents the super-Nyquist signal from being aliased back into the sub-Nyquist range. Useful lens-sampling combinations with no aliasing are indicated in the last column in green.

Table 1 - Sampling parameters for all possible combinations of lens magnifications for the NewView™-9000 profiler in the ALS XROL lab.

		MTF cutoff fNA λ=550nm				Pixel sampling						
Objective magnification	NA	period [um]	fNA MTFcutoff [um-1]	Zoom	Effective magnification	projected pixel size [um]	Total trace length [um]	Fundamental freq [um-1]	samp fNy Nyquist freq [um-1]	sampling Nyquist period [um]	fNA MTFcutof / samp fNy	Aliasing? fNA < samp fNy
2.75	0.08	3.438	0.291	0.5	1.375	6.31	6312.73	0.000158	0.079	12.63	3.67	YES
Michelson			**0.291**	**1**	**2.75**	**3.16**	**3156.36**	**0.000317**	**0.158**	**6.31**	**1.84**	YES
			0.291	2	5.5	1.58	1578.18	0.000634	0.317	3.16	0.92	NO
10	0.30	0.917	1.091	0.5	5	1.736	1736	0.000576	0.288	3.472	3.79	YES
Mirau			**1.091**	**1**	**10**	**0.868**	**868**	**0.001152**	**0.576**	**1.736**	**1.89**	YES
			1.091	2	20	0.434	434	0.002304	1.152	0.868	0.95	NO
20	0.40	0.6875	1.455	0.5	10	0.868	868	0.001152	0.576	1.736	2.53	YES
Mirau			**1.455**	**1**	**20**	**0.434**	**434**	**0.002304**	**1.152**	**0.868**	**1.26**	YES
			1.455	2	40	0.217	217	0.004608	2.304	0.434	0.63	NO
50	0.55	0.5	2.000	0.5	25	0.347	347.2	0.002880	1.440	0.6944	1.39	YES
Mirau			**2.000**	**1**	**50**	**0.174**	**173.6**	**0.005760**	**2.880**	**0.3472**	**0.69**	NO
			2.000	2	100	0.0868	86.8	0.011521	5.760	0.1736	0.35	NO

2.1 Ideal BPRG parameters

When we make a measurement of the 2D surface topography with an interferometric microscope, the data points are arranged on a rectangular grid and are usually analyzed by computing the average 1D periodogram estimator of the PSD on a row-by-row or column-by-column basis. Each row PSD is averaged into one that represents the spectral distribution of roughness in that direction. To examine the effects of resampling with different pixel pitch and with sub-pixel shifting, it is more convenient from a computational efficiency standpoint to use a 1D model of the BPRA that contains all of the features necessary to simulate the 2D observations. The 1D version of the BPRA, the binary pseudo-random grating (BPRG) was the predecessor of the BPRA and is discussed in earlier references.[22, 23] For illustration purposes, we use the 1D URA pattern with 2^{12}-1 = 4095 elements generated according to the method in Koleske and Sibener[27] shown in Fig. 2. The mean has been removed from the binary 1-0 height distribution, so the illustrated points have ±1/2 values. The autocovariance function (ACF) of this profile is a single spike at zero lag, indicative of a white noise-like profile. The periodogram estimate of the PSD function for this profile is a constant, confirming that the generated profile has the desired properties. The root-mean-square (RMS) value for this binary pattern is 0.5, and the value of the ACF at zero-lag is the square of this number, 0.25, as it should be.

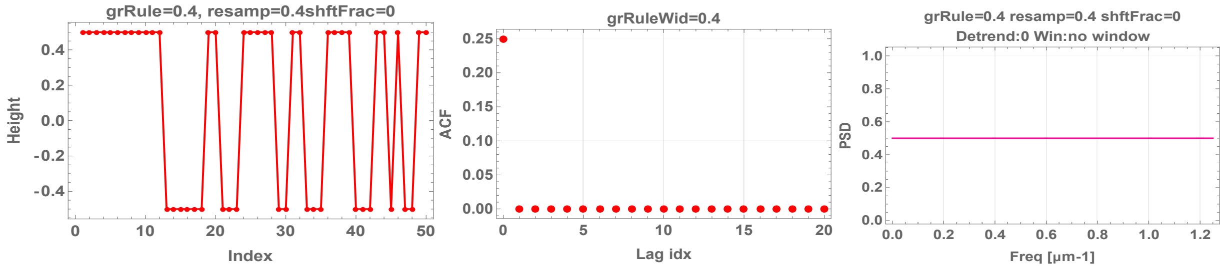

Figure 2 - (Left) First 50 elements of the BPRG height profile for the mathematically ideal case, with the mean subtracted. The RMS is 0.5. (center) Autocovariance function of the height showing a delta-function-like spike at zero lag. The remainder of the points are below the 10^{-3} level;.(right) Periodogram estimate of the PSD is constant, indicative of a white-noise profile. The frequency is scaled to 0.400μm ground rules.

2.2 Resampling

When we make a real measurement of a BPRG, it is practically impossible to match the magnification of the microscope to the grid spacing of the base BPRG to align all elements exactly along the boundaries of the camera pixels. This is a pathological alignment case – it never occurs in practice. The general case has the magnified camera pixels straddle transition boundaries between feature elements on the base BPRG. The binary height distribution is then split between adjacent pixels in the camera. This is the resampling process. We use an algorithm that resamples the initial base BPRG to a grid with larger or smaller size pixels by integrating the base heights within each projected pixel region. The resampled pixel amplitude is then normalized to the new pixel pitch. The total physical length of the resampled profile does not change, but the number of sampled pixels varies according to the resampled pixel size. This aspect of the simulation differs from the actual measurement of a BPRA, where the total number of points remains constant (1000x1000) as the size of the region viewed in the image changes. In the simulation, since the total length of the resampled profiles remains constant, the fundamental frequency in the sampling remains constant, while in the real measurement case, the fundamental frequency changes as the area changes. This difference between the simulation and the physical measurement is inconsequential, as the spectrum at the low frequency end is essentially constant in both cases. Fig. 3 shows the result of resampling for the two cases: undersampling (upper row), where the resampled pixel pitch is greater than the base pattern ground rules, and oversampling (lower row), where the resampled pixel pitch is less than the base pattern ground rules. In general, we have found that the undersampled PSDs (upper row) can be described by a cosine function, while the oversampled PSDs are described by a sinc-squared function. This will be discussed further below. We note that the typical PSD computed from the resampled data is no longer a smooth curve: it is noisy because the resampling pitch is generally not an integer multiple of the ground rule pitch and it is only a single realization of a resampled BPRG. It is not averaged with other BPRG pattern realizations. Other n=12 binary URA patterns are possible and will be implemented in future simulations. In the case of a real measurement with the interference microscope, each row in the image is treated as a separate realization and then all of the resulting PSDs can be averaged to reduce the variance in final PSD.

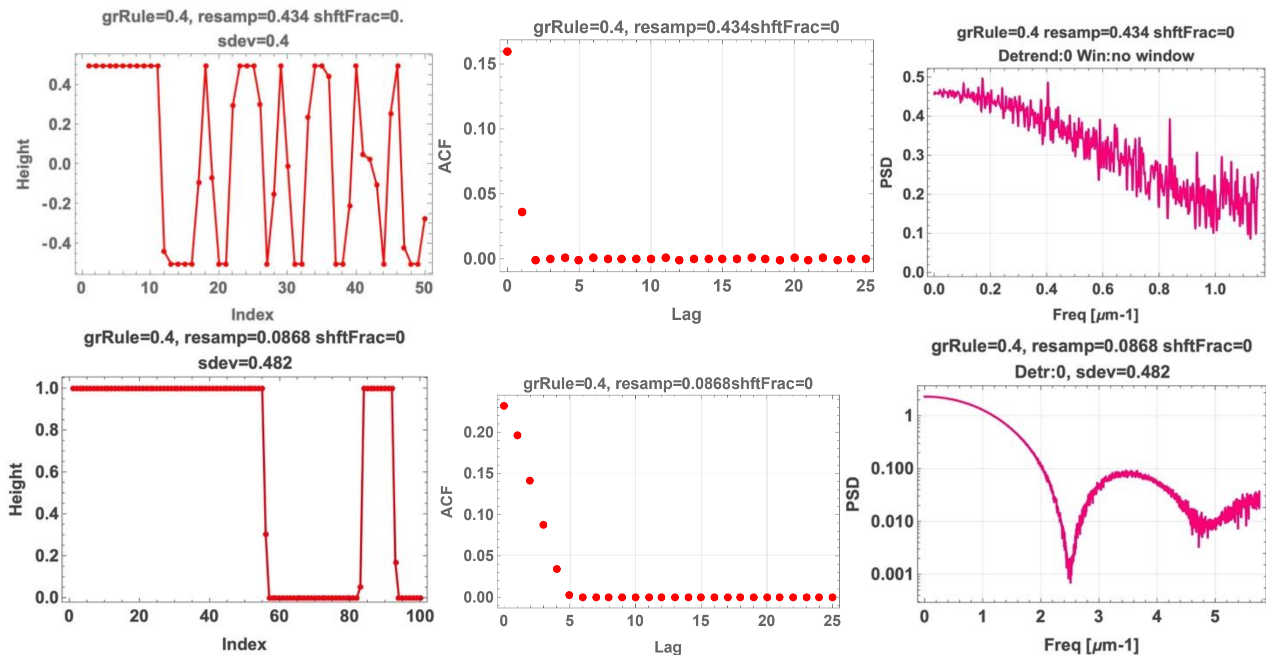

Figure 3 - Resampled 400nm BPRG with autocovariance function and PSD: (upper) undersampled with 434nm pixels, corresponding to a 20x1x objective-zoom combination; (lower) oversampled with 86.8nm pixels, corresponding to a 50x2x combination. The lag length is the resample pixel pitch in each case.

Table 2 shows the ratios of the projected pixel pitch to the base pattern ground rule pitch (grRule) for all of the lens magnification-zoom combinations available for the microscope with 8.68μm pixels on a 1000x1000 grid. The ratio of projected pixel pitch to the ground rule pitch determines the over- or under-sampling condition: ratios greater than 1 are

undersampled, ratios less than 1 are oversampled. We note that the oversampled PSDs always have a null in the spectrum before the Nyquist frequency of the sampling array, while the undersampled PSDs do not.

Table 2 - Ratio of projected pixel pitch to the base BPRA pattern ground rule pitch for a microscope with 8.68μm pixels. Ratios greater than 1 are undersampled (green squares), less than 1 are oversampled.

			pattern ID	D	C	B	A
			grRule size [nm]	400	800	1200	2500
			grRule null f [um-1]	2.5	1.25	0.833	0.4
projected pixel size [um]	Aliasing? fNA < samp fNy	Objective magnification	Zoom	**Ratio: proj pix / grRule size undersampled > 1 oversampled < 1**			
6.313	YES	2.75	0.5	15.782	7.891	5.261	2.525
3.156	YES	Michelson	**1**	7.891	3.945	2.630	1.263
1.578	NO		2	3.945	1.973	1.315	0.631
1.736	YES	10	0.5	4.340	2.170	1.447	0.694
0.868	YES	Mirau	**1**	2.170	1.085	0.723	0.347
0.434	NO		2	1.085	0.543	0.362	0.174
0.868	YES	20	0.5	2.170	1.085	0.723	0.347
0.434	YES	Mirau	**1**	1.085	0.543	0.362	0.174
0.217	NO		2	0.543	0.271	0.181	0.087
0.347	YES	50	0.5	0.868	0.434	0.289	0.139
0.174	NO	Mirau	**1**	0.434	0.217	0.145	0.069
0.0868	NO		2	0.217	0.109	0.072	0.035

2.3 Oversampling

Figure 4 (left) shows the 4 simulated PSDs computed for the 4 oversampled combinations indicated at the bottom of the 400nm ground rule column in Table 2. The curves are labeled by the pixel sampling pitch, ranging from 347nm down to 86.8nm for objective-zoom combinations of 50x0.5x, 20x2x, 50x1x, and 50x2x, or total magnifications of 25x, 40x, 50x, 100x, respectively. Along with these simulated oversamplings, the sinc-squared function is shown using the 400nm grRule pitch as the periodicity parameter. One can see from the curves in Fig. 4 that the simulated PSDs are described precisely by a single sinc-squared function with the periodicity parameter set to the ground rule pitch. The sinc-sq function is given by

$$\text{sinc-sq} = \left(\frac{\sin\left(\pi\, grRule\, f\right)}{\pi\, grRule\, f} \right)^2 \tag{1}$$

The oversampled height profile in the bottom left in Fig. 3 is similar to the random telegraph signal discussed by Rice in his treatise on random noise processes.[34, 35] He shows that a sampled binary signal has a correlation function given by a ramp function: $\left(1-\frac{|x|}{h}\right)$ for |x| $<h$ and is 0 otherwise, where h is the correlation length. This correlation function (ignoring normalization factors) has a spectrum given by the sinc-sq function in eqn. (1). We can see from Fig. 3 (lower center) that the oversampled ACF with lags equal to the resampled pixel pitch can be described by a ramp function with h = grRule pitch, with the corresponding PSD described by the sinc-sq function.

Note that these PSDs show the frequency response only for the pixel sampling function and do not include lens cutoff or other system response considerations. If the lens cutoff for the 50x objective at f = 2.0μm^{-1} is imposed, the curves beyond 2.0μm^{-1} would drop to the noise level or to effectively zero. In any case, using the measured oversampled PSD from the 400nm BPRA pattern for ITF investigations is problematic because of the large amplitude difference between

low and high frequencies. Also shown in Fig. 4 (right) are actual measurements on the A-pattern that has 2.5μm ground rules, along with the corresponding sinc-sq function. One can see from the A-column in Table 2 that these magnification combinations are all greatly oversampled. The sinc-sq function with grRule = 2.5μm describes the sampling nulls exactly for these measurements.

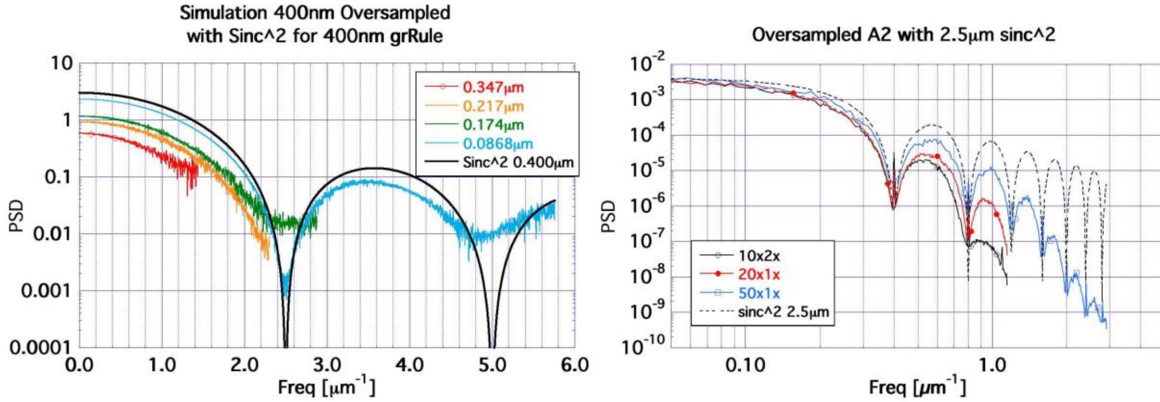

Figure 4 – (Left) PSDs for simulated oversampled 400nm BPRA for the indicated resampling pixel pitch. The sinc-sq function for 400nm grRule is also shown. (Right) Actual measured PSDs for the A2 pattern with 2500nm ground rules, with the sinc-sq function for this ground rule pitch.

2.4 Undersampling

Table 2 highlights in green all magnification-ground rule pattern combinations that are undersampled. Simulated PSDs for selected projected pixel pitches for each of the four ground rule patterns are shown in Fig. 5. A 2-parameter cosine function is fit to each PSD using the relevant resampled pixel pitch value as the periodicity, *per*:

$$PSD = A + B\cos\left(2\pi \cdot f \cdot per\right) \tag{2}$$

Since the undersampled pixel pitch is always greater than the grRule pitch, the Nyquist frequency of the PSD never exceeds the frequency corresponding to the grRule pitch, hence the value of the cosine fit never goes to zero. The green entries indicate those magnification-ground rule combinations that provide useful frequency range coverage. This is illustrated in Fig 5 for the different magnification combinations for each of the grRule values. The smallest size resampled pixel PSD falls off more steeply than the others at high frequencies because its sampling period is closer to the ground rule period than for the other PSDs. For ITF calibration purposes, the flatter curves are more useful because they do not fall off so much at high frequency. In Table 2, combinations with resampled pitch-to-ground rule pitch ratios greater than 2 will be most useful for calibrations. Except for magnifications greater than 25x, for a given magnification, there are at least one or two BPRA patterns with ground rules that have PSDs useful for ITF calibration. Higher magnifications require a BPRA pattern with ground rules smaller than 400nm, such as with the HR BPRA with smallest ground rules of 80nm. The amplitudes of the PSDs for a given ground rule pattern are proportional to the height values of the resampled profiles. Resampling with larger pixel pitch is a low-pass smoothing operation resulting in smaller values for the resampled heights, hence lower rms and PSD numbers.

The low frequency ends of the simulation PSDs are determined by the length of the initial BPRG profile, which is the number of points, 4095, times the ground rule pitch. The 800nm grRule low frequency limit is lower than that of the 400nm grRule because the simulated 800nm profile is “longer” The other larger grRule patterns have even lower fundamental frequencies. In actual use, when a BPRA is viewed at a particular magnification, its truncated field of view is always smaller than the full extent of the BPRA, so its low frequency limit is determined not by the intrinsic size of the array, but only by the size of the field of view. When that same BPRA is viewed at a different magnification, the area size changes and the fundamental frequency changes. The high frequency Nyquist limit is determined solely by the resampled pixel size, which remains constant as the total trace length is changed. Except for the lowest magnification with the A-pattern, all the magnification entries in the table have a field of view that lies entirely within the intrinsic BPRA patterns.

The simple cosine function in equation 2 with coefficients in the ratio of A=2B appears to describe most of the simulated PSDs in Fig. 5. Because of the large variance in the PSDs at high frequencies, the differences between fits with the period parameter equal to the ground rule pitch or to the resampled pixel pitch are very small. Further study is needed to determine the proper form of the undersampled ideal PSD. For the present analysis, where we need to start with a normalized PSD, we set the coefficients to A=2/3 and B=1/3.

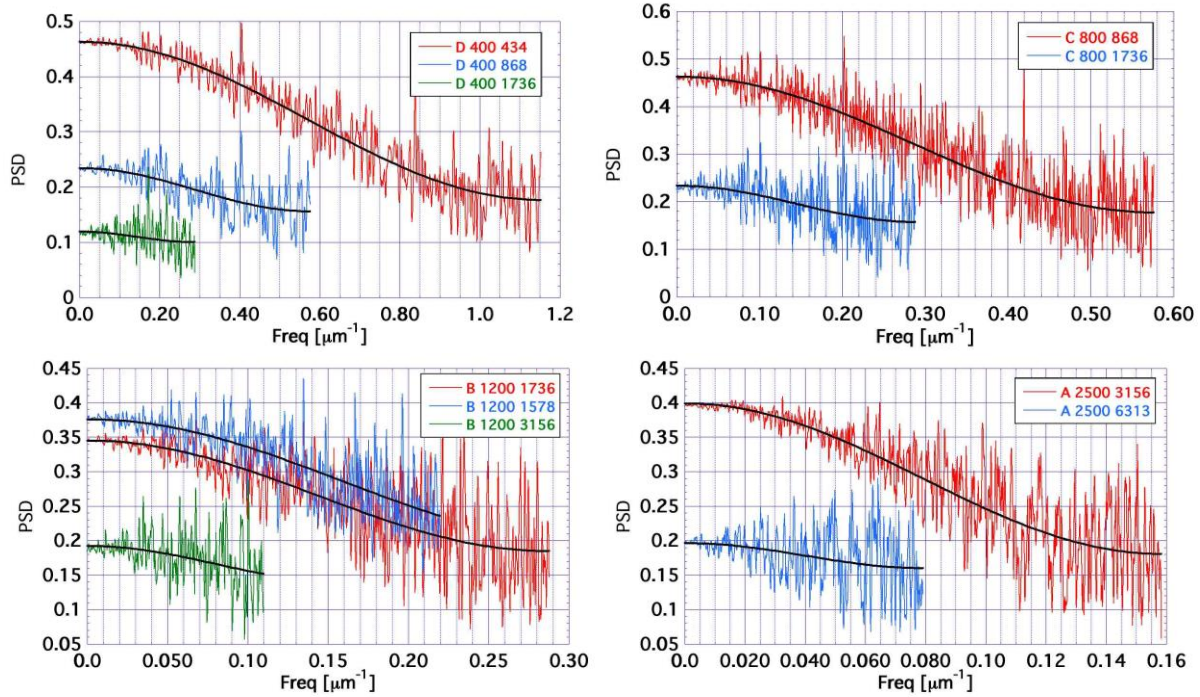

Figure 5 – PSDs for the 4 different ground rule pitch resampled to larger pixel pitch as indicated, i.e. undersampled. The cosine function fit to each PSD is superimposed on each curve. The ratio of A to B coefficients is found to be 2 to1 empirically.

2.5 Non-shift invariance issues

It is well-known in digital signal processing that sampled images are not linear shift invariant.[36] For binary intensity objects, the MTF of the measured pattern depends on the fractional sub-pixel position of a transition edge within a given pixel. The ISO 15529 standard discusses the issues involved in defining an average MTF for non-shift invariant sampled imaging systems based on slanted edge or line patterns.[37] Interferometric microscope measurements of step-edge phase-shifting patterns suffer the same shift invariance issues. We can use our resampling model to explore shift invariance issues of BPRA measurements.

We illustrate non-shift invariance by keeping the pixel size constant at 400nm, but shifting the entire pattern by fractions of a pixel so it is not exactly aligned with the sampling grid. Because the original array is a distribution of 1s and 0s precisely aligned to a grid, the pixels at the transition boundaries now have intermediate values that depend on the amount of the shift, as illustrated in Fig. 6. The corresponding PSDs for these shifted profiles are shown in Fig. 7. In a fashion similar to the slanted edge MTF curves, the shifted BPRG PSDs oscillate between unity and zero at high frequency. For a shift of 0.5 pixels, Fig. 6(d), the transition pixels all have a value of 0.5 and the PSD has a null at the Nyquist frequency. This case is pathological, in that this particular pattern alignment to the camera grid will never happen during a typical measurement scenario. The general case is that the BPRA will have a random distribution of transition edges among the resampled pixels, and the resultant PSD will be an average over all the oscillating PSDs. We illustrate the general fractional shift case in Fig. 8 with PSDs for the 400nm BPRG resampled to 434nm pixels, corresponding to a measurement with a 10x2x or 20x1x objective-zoom combination. The PSDs of the resampled pattern for fractional shifts in increments of 0.1 pixel over the 0.0 and 1.0 pixel shift range are superimposed along with the average of the 11 individual PSDs. The PSDs for each of the fractional shifts are essentially identical, showing that the

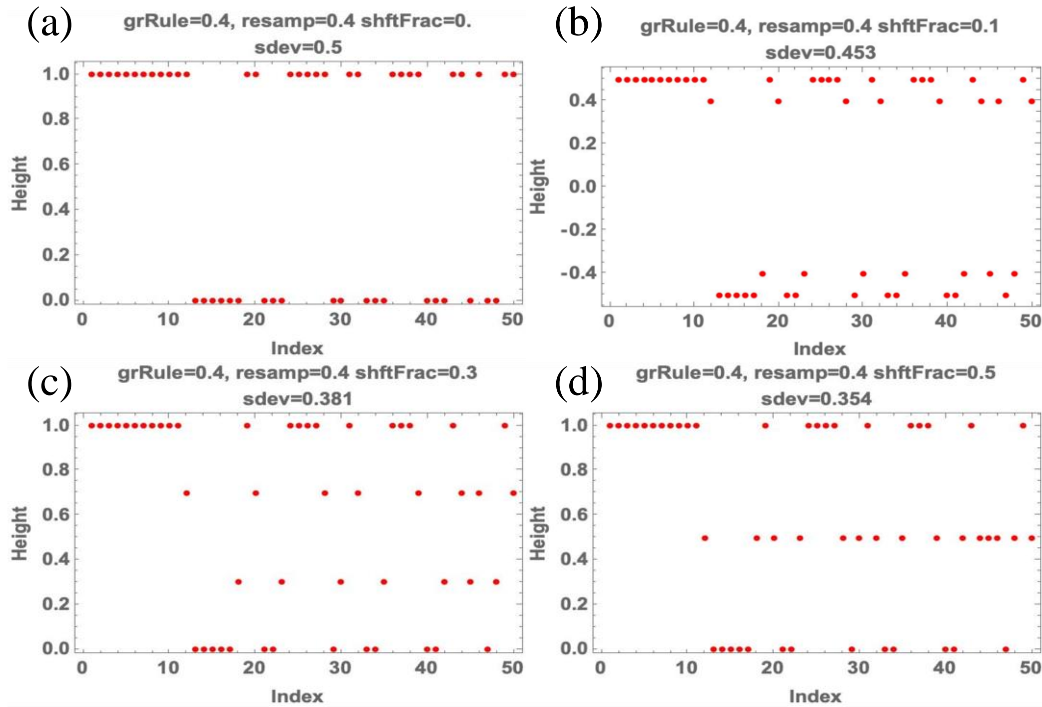

Figure 6 - Fractional pixel shifts, keeping the pixel size constant. The transition boundary pixels are affected by the shifting. (a) Intrinsic array, no shift; (b) Shift = 0.1 pixel; (c) Shift = 0.3 pixel; (d) Shift = 0.5 pixel.

non-shift invariant transition pixel effects are averaged out when the resampled pixel size is different from the intrinsic BPRA ground rules.

Another extreme example of randomization of shift invariance is seen when the pixel resampling size is increased by just a very small amount, from 400nm to 401nm. The resampled pixel intensities for the first 500 pixels are shown in Fig. 9 along with the PSD computed from this profile. There is a regular progression in the increase or decrease in transition edge pixel

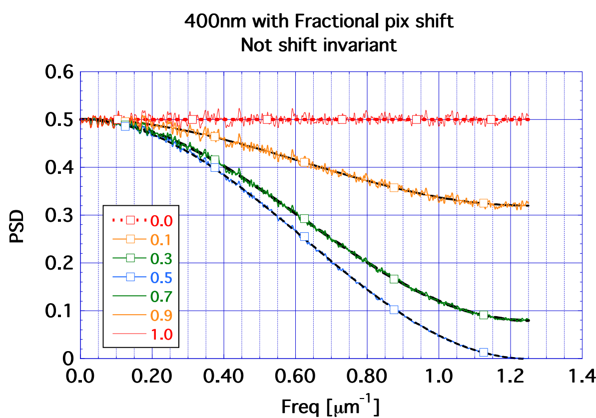

Figure 7 – PSDs for the 400nm BPRG pattern shifted by fractions of a pixel width. Non-shift invariance is manifested by the different shapes of the curves as the transition edges traverse a distance of one pixel. PSDs are symmetric about the 0.5 shift value.

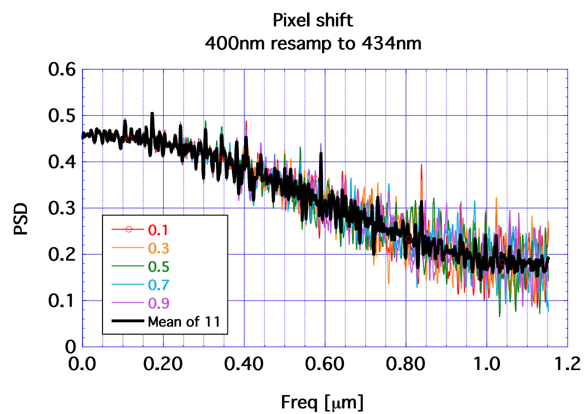

Figure 8 - PSDs for 400nm BPRG resampled to 434nm and shifted by the indicated fractional pixel. The average of all 11 PSDs is also shown. All are essentially identical, indicating the non-shift invariance is averaged out by the resampling.

values in this case, similar to a vernier scale. There are a little more than 10 cycles of this regular 401 pixel long pattern in the full resampled profile but the resultant PSD shows that the pathologicality of the non-shift invariant PSDs has been averaged out, since the PSD in Fig. 9 is similar to that in Fig. 8. We can conclude that, except for the pathological case, because the resampled BPRG has transition edge positions distributed randomly between the initial array ground rule positions, the resultant PSD will behave like the average over all the pathological PSDs. Since this holds for the 1D grating BPRG, we expect it to be true for the 2D BPRA.

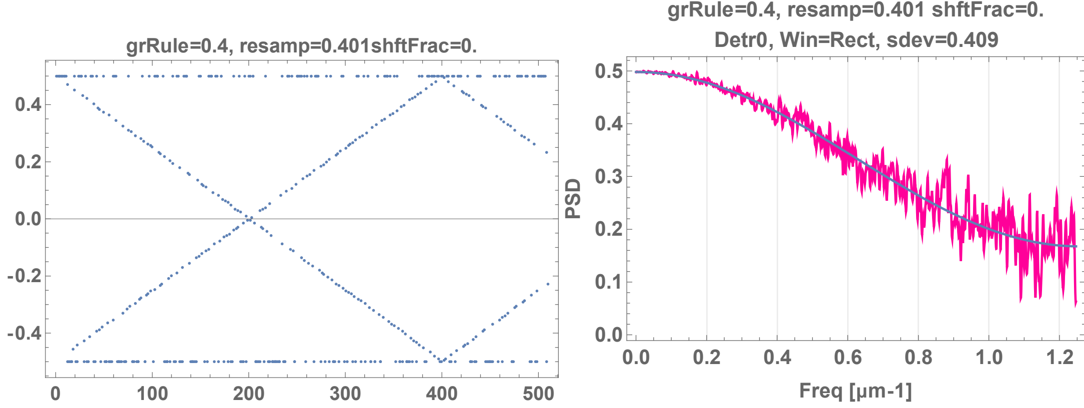

Figure 9 – (Left) The first 500 points in a resampling of a 400nm pattern to 401nm pixels. The regular progression of pixel height values over 10 cycles in the 4K long pattern is enough to average out the non-shift invariant behavior of the PSD, (right) which is the same as that in Fig 8 for the 434nm resampling.

3. ITF MODELING BASED ON MEASUREMENTS WITH THE BPRA

The usefulness of a BPRA in assessing the ITF of optical instruments arises from its predictable spatial frequency spectrum. We can use it to model the expected PSD that we should observe when we make a measurement with an interferometric microscope. The difference between the model and the observed PSDs we attribute to attenuation by the ITF of the measuring instrument. In order to model the ITF of the microscope, we need to consider the various components that comprise the transfer function of the microscope. de Groot gives a comprehensive review of all of the considerations that go into determining the ITF of interference microscopes.[20] We use a simplified linear model that considers only the transfer functions of the lens and detector pixels.[18] The measured PSD, S_{meas},is given by

$$S_{meas}(f) = M_{inst}^2 S_{obj} \tag{3}$$

where S_{obj} is the intrinsic spectrum of the height topography of the object and M_{inst} is the ITF.

We use a simple model where the MTF of the microscope is given by the product of the incoherent lens MTF and the pixel sampling MTF:

$$M_{model} = M_{lens} M_{pix} \tag{4}$$

The lens MTF depends on the numerical aperture, NA, and the wavelength, λ:[38]

$$M_{lens}\left(f\right) = \frac{2}{\pi}\left[\cos^{-1}\left(\frac{\lambda f}{2NA}\right) - \frac{\lambda f}{2NA}\sqrt{1-\left(\frac{\lambda f}{2NA}\right)^2}\right] \tag{5}$$

and the pixel sampling MTF is given by the sinc function:

$$M_{pix}(f) = \frac{\sin\left(\pi f d\right)}{\pi f d} \tag{6}$$

where d = pixel width and is also the sampling period of the magnified camera grid. The lens MTF goes to zero at $f_{cutoff} = \frac{2NA}{\lambda}$ and acts as a low pass filter to cut off the object's frequency components beyond this frequency. The Nyquist frequency corresponding to the pixel sampling period is fNy = 1/(2d). If the lens cutoff frequency is less than fNy, then there is no aliasing of higher frequencies back into the sub-Nyquist range. If the lens cutoff frequency lies beyond fNy, then the observed signal is contaminated by super-Nyquist power and needs to be addressed.

The lens transfer function in eqn. (5) is derived for a simple circular aperture. The Mirau objectives in the NewView system have obstructions in the center of the aperture that modify the frequency response. We have incorporated into our model the correction factors derived by O'Neill for systems with annular apertures.[39, 40] The relative obstruction ratio is a parameter in our model that we can invoke to improve the fit of our model to the measured data, as we currently have no *a prioi* knowledge of what the central obstruction ratios are for our objectives.

When we apply the model MTF to the PSD computed for the BPRA, we get the expected model PSD, S_{model}:

$$S_{model} = M^2_{model} S_{BPRA} = M^2_{lens} M^2_{pix} S_{BPRA} \tag{7}$$

When we measure a BPRA, we have a measured PSD, S_{meas}. The ratio between the measured and model PSDs tells us how good our model is at describing the ITF:

$$\frac{S_{meas}}{S_{model}} = \frac{M^2_{inst} S_{obj}}{M^2_{model} S_{BPRA}} \tag{8}$$

But, to the extent that we have modeled the PSD of the BPRA correctly, S_{obj}=S_{BPRA}, and the ratio becomes

$$\frac{S_{meas}}{S_{model}} = \frac{M^2_{inst}}{M^2_{model}} \tag{9}$$

The deviation of this ratio from unity gives us insight into deficiencies in our simple model and what we might need to consider to improve upon it.

Our lens transfer function model also includes a defocus term, based on equations 42 and 43 in the paper of Simonov and Rombach.[41] Their expression is valid for small values of defocus. We have found that there has been no need to invoke the defocus term in the current modeling of the NewView objectives, as they all appear to be in good focus, and the heights of the BPRA artifacts are all well within the nominal depth-of-focus range given by $\Delta z \approx \lambda / 2NA^2$ for all objectives. Also, in coherence scanning mode, which was used in the present measurements, the surface feature is always at the nominal focus position of the vertically scanned lens, so we don't expect to see any defocus in the measured height profiles. Only if the objective were to be grossly misaligned, so that the null in the interferometer OPD deviates significantly from the position of best focus, would we need to consider using the defocus term.

4. COMPARING MODELS TO MEASUREMENTS

The measurements used to compare with the modeled PSDs were made with a NewView-9000 interferometric microscope on a BPRA artifact with parameters shown in Fig. 1. The details of the instrument and the measurement conditions are presented in a related paper at this conference.[42] The measurements were made on the A2 to D2 patterns, which are the highly randomized version of the BPRAs, in coherence scanning interferometer mode (CSI).

4.1 20x 1x zoom with 400nm BPRA

The 20x1x objective has a lens cutoff frequency of 1.455μm^{-1} and a Nyquist frequency of 1.152μm^{-1}. Fig. 10 shows the MTF^2 curves for 0.434μm size pixels (red) and the lens NA (blue), along with the intrinsic spectrum for this pattern according to the cosine function in eqn (2). Because the lens cutoff is beyond the Nyquist frequency of the array, there will be some aliasing of the BPRA PSD from the super-Nyquist region back into the sub-Nyquist region. However, the magnitude of the aliased power will be very small, as it will be highly attenuated by the small lens MTF in the super-Nyquist region.

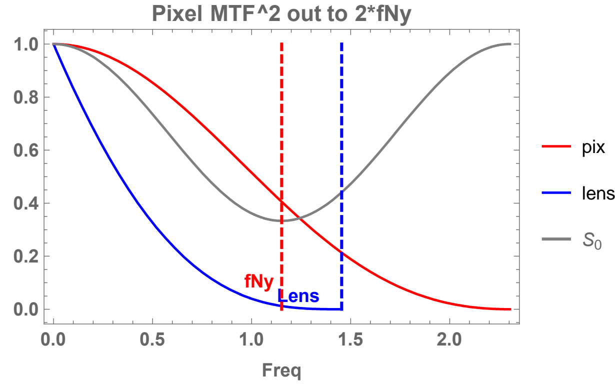

Figure 10 - MTF^2 curves for resampled 0.434µm pixels (red) and the lens response (blue) for the 20x objective with 1x zoom. Also shown is the cosine function that describes the normalized intrinsic spectrum, S_0, (gray), for the resampled pixel width.

When the intrinsic spectrum is multiplied by the pixel and lens MTFs, with the aliased contribution included, the result is the predicted spectrum of what we should see in the actual measurement. The individual aliased components are plotted in Fig. 11 along with the combined MTFs applied to the intrinsic spectrum. The combined spectrum (orange) is the model spectrum that we compare to the measurement, shown in green as discrete points. The model functions are all normalized to unity at zero frequency. We need to normalize the measured PSD in order to compare it to the model results. One can see from scatter in the measured points at low frequency that there is some uncertainty in what the zero frequency value might be due to the inherent variance in the periodogram estimator that we use to calculate the PSD. We make the assumption that the "true" PSD is a smooth, monotonically decreasing function and fit the low frequency points to a 2nd order polynomial to extrapolate to f=0. This gives us the normalization factor for the measured curve.

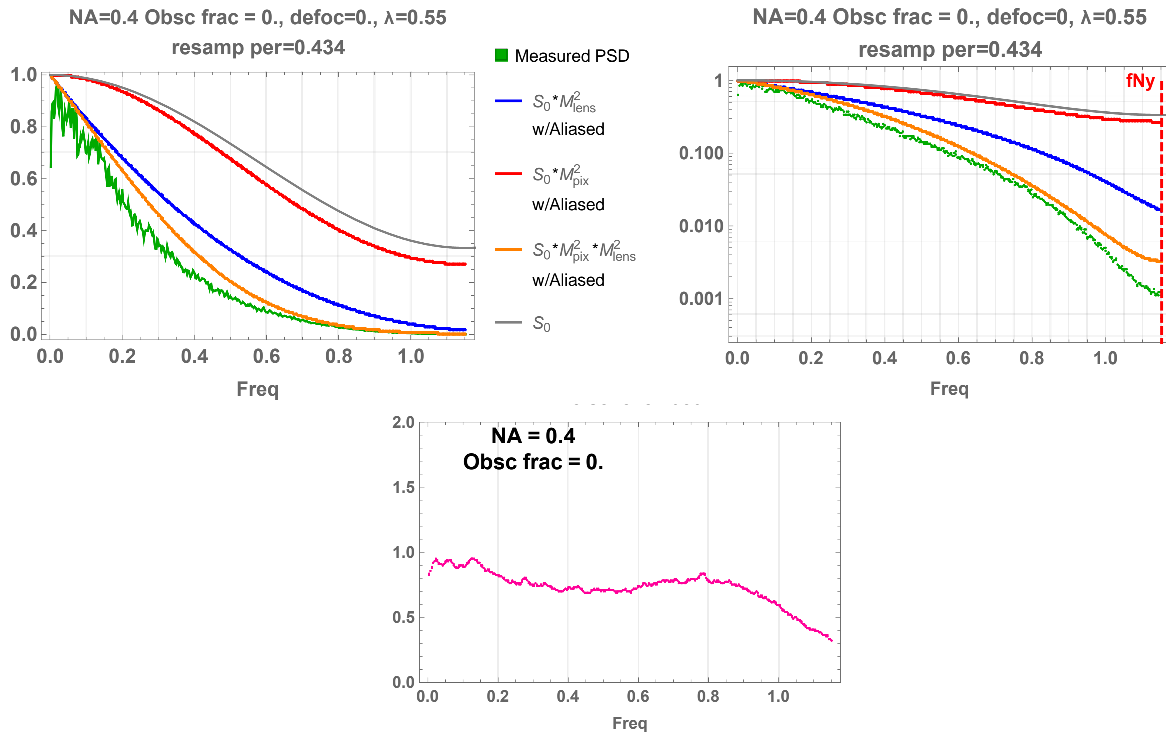

Figure 11 – (Upper) The MTFs of the lens and pixel sampling (blue and red curves) multiply the intrinsic PSD for the 20x1x model with 0.434µm resampled pixels, resulting in the orange curve. This is compared to the actual measured points (green).(Lower) Ratio of measured PSD to the model curve. The ratio is less than unity over the whole frequency range.

One can see that the normalized, measured curve (green) lie below the model curve (orange) over the entire frequency range. The ratio of measured to model on the right in Fig. 11 shows the deviation of the model from the data. That the model curve lies above the measured data suggests that we need to consider the central obscuration factor in the lens MTF. The effect of the central obscuration is to reduce the lens MTF over the middle frequency range. By trial and error, the value of the obscuration parameter that gives the best fit by eye is 0.23. This model fit is shown in Fig. 12 as the orange line. It fits the model curve over the lower half of the frequency range quite well. This is clearly shown in the ratio between the measured and modeled curve (lower). The falloff of the ratio at higher frequencies indicates a divergence between the model and measurement that is not yet accounted for. The model PSD is too high at these frequencies. Aliasing only affects the very end of the model PSD, producing the slight hook that is visible and cannot account for the difference from the measured PSD at frequencies beyond 0.8μm^{-1}.

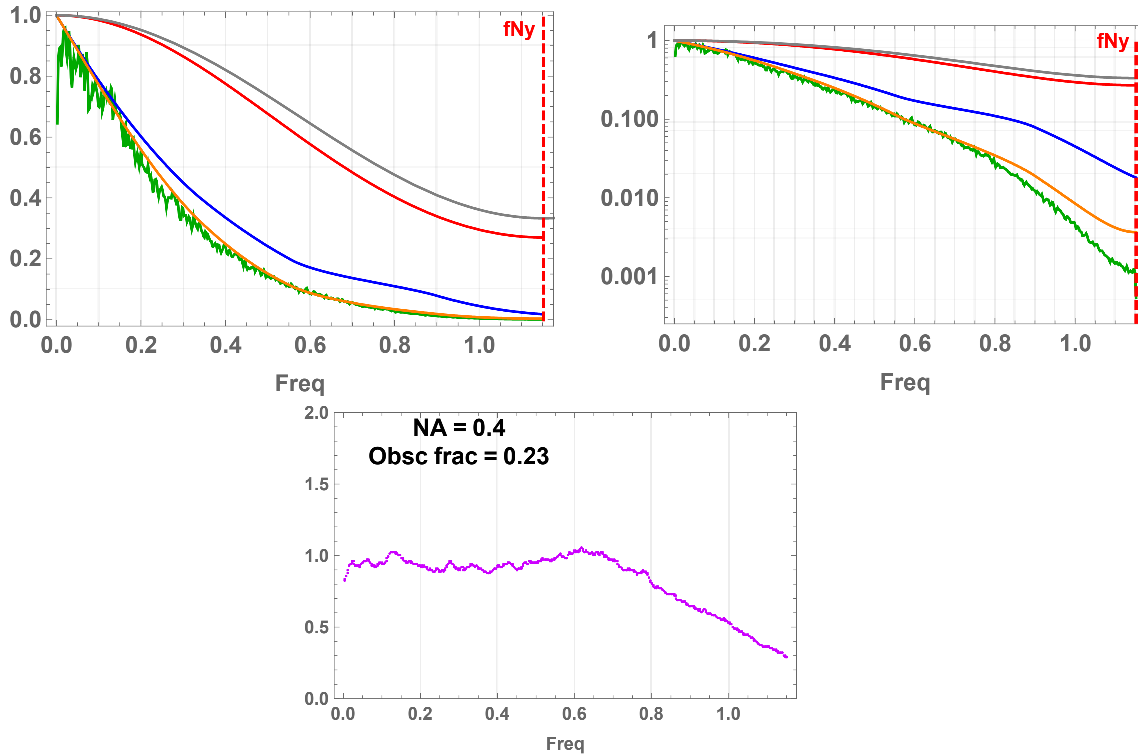

Figure 12 – (Upper) Adding an obscuration factor of 0.23 to the lens MTF brings the model curve (orange) down closer to the measured data (green). The legend labels are the same as in Fig. 11. (Lower) The ratio between measured and modeled PSDs is unity over the lower half of the frequency range but diverges at high frequencies. The model does not fall off as fast as the measured PSD.

4.2 10x 2x zoom with 400nm BPRA

The 10x objective has a nominal numerical aperture of 0.3 that is smaller than the 20x NA of 0.4, hence its cutoff frequency is lower at 1.091μm^{-1}. But the objective magnification and zoom factor combine for an overall magnification of 20x, which is the same as the 20x objective with the 1x zoom discussed in the previous section. The projected pixel size and Nyquist frequencies are the same for both cases because the overall magnifications are the same: 0.434μm with a Nyquist frequency of 1.454μm^{-1}. But the lens cutoff frequency now lies before the Nyquist frequency, so there will be no aliasing of any power from the super-Nyquist region back to the sub-Nyquist region for the 10x2x objective. When we run the model with these parameters and compare the results to the measured PSD, we get the results shown in Fig. 13 (top row). What is most evident is that the measured PSD (green) drops off much faster than the model with NA=0.3 for the 10x objective, with the assumption that the addition of the 2x zoom lens does not affect the NA. The ratio between measured and model PSDs in Fig. 13 for NA=0.3 drops below unity for midfrequencies, then blows up at high frequencies due to the apparent noise floor beyond 0.8μm^{-1}.

Now we adjust the NA value in the model to see if we can get a better fit to the data at the higher frequencies. We also subtract the mean noise floor value for the frequencies beyond 0.8μm^{-1}. Fig 14 shows the ratios of measured to model PSDs as the NA value varies from 0.25 to 0.27. One can see that the NA=0.27 provides the best fit over the low- and mid-frequency range. The model PSD is shown on the right for NA=0.27 (orange) with the noise floor subtracted from the measured PSD (light green). The fit is quite good for normalized PSD values between 1.0 and 0.01 but diverges as before for PSDs below the 1% level as the Nyquist frequency is approached. So we can conclude that the addition of the 2x zoom lens to the 10x objective changes the NA from 0.3 to 0.27 and lowers the lens cutoff frequency from 1.091μm^{-1} to 0.982μm^{-1}. Note that in this model, the obscuration factor remains at 0.0. We do not need to invoke obscuration to get a good model fit.

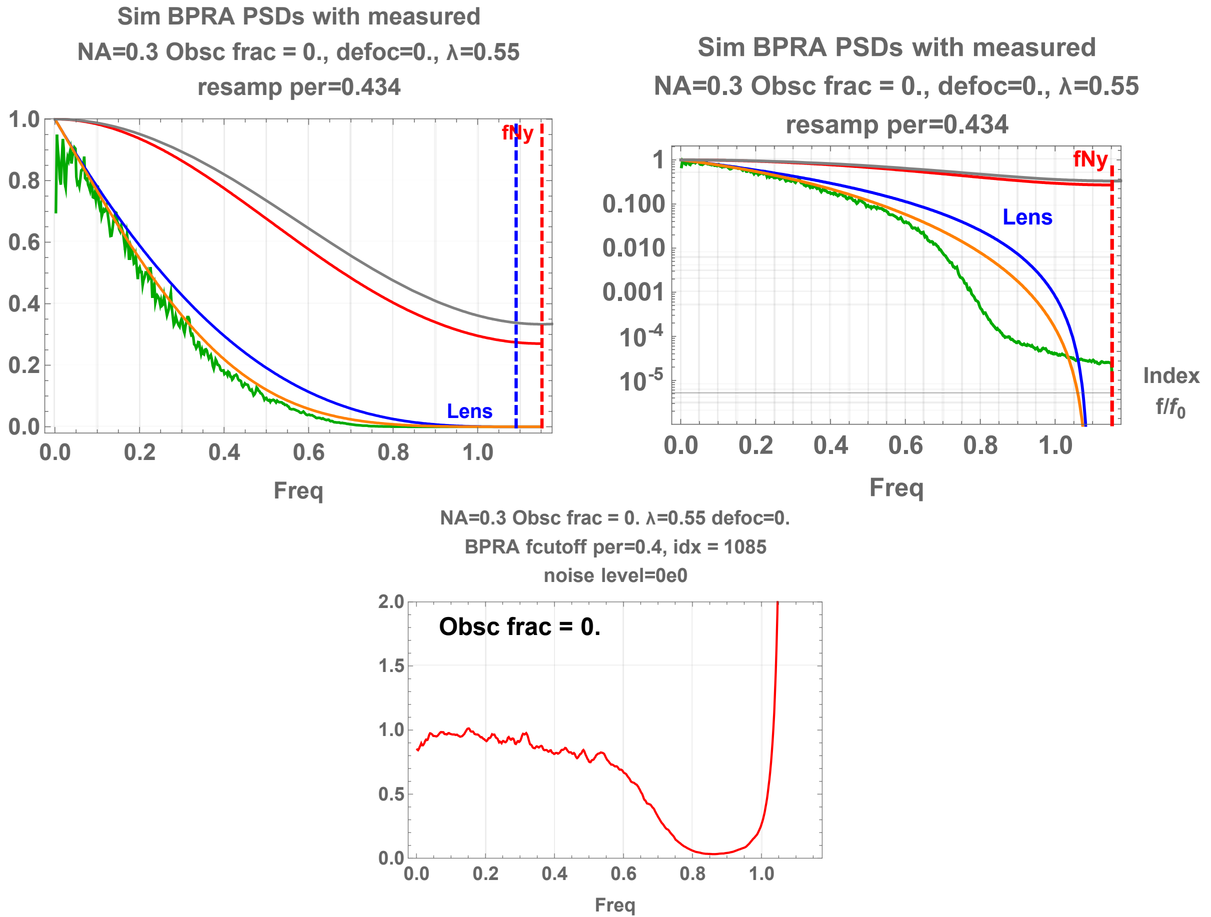

Figure 13 – (Upper) 10x objective with 2x zoom. Lens cutoff frequency is before the Nyquist frequency, so no aliasing occurs. The dropoff of the measured PSD beyond 0.5μm^{-1} suggests an internal aperture restricting the higher spatial frequencies. (Lower) The bottom row plot is the ratio of measured to model PSDs. The noise floor at high frequencies causeds the ratio to blow up there.

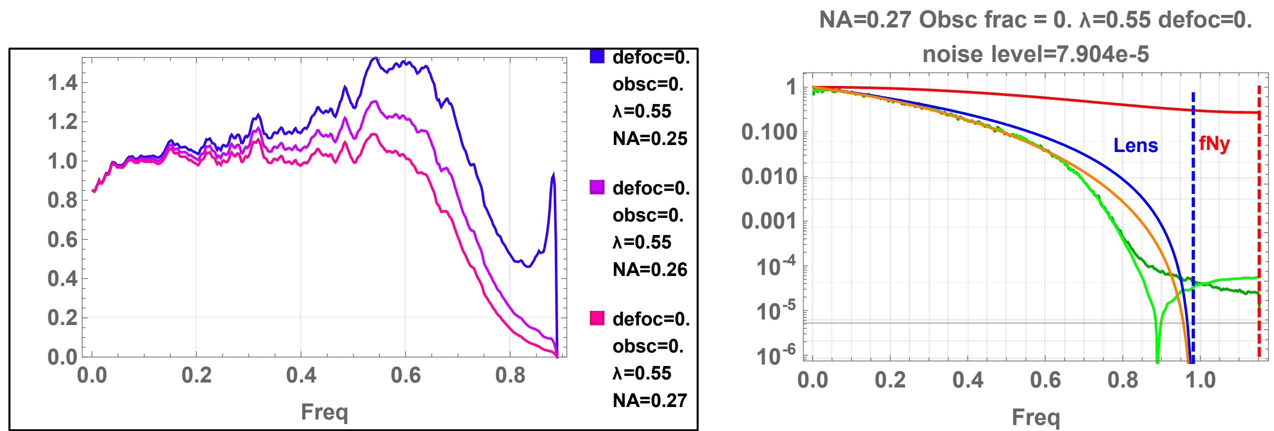

Figure 14 – (Left) Ratio of measured to model PSDs as NA is varied from 0.25 to 0.27. NA=0.27 provides the best fit for the 10x2x objective-zoom combination. (Right) Noise floor subtracted from measured data (light green) with NA=0.27 model fit (orange).

4.3 10x 1x zoom with 400nm BPRA

The 10x 1x zoom lens combination has a magnification of 10x with resampled pixels of 0.868µm with a Nyquist frequency of is 0.576 μm^{-1}. The nominal NA of this lens is 0.3 with a lens cutoff frequency of 1.091μm^{-1}. Since the Nyquist frequency is lower than the lens cutoff, we expect some aliasing to occur. The model and measured PSD curves are shown in Fig. 15.

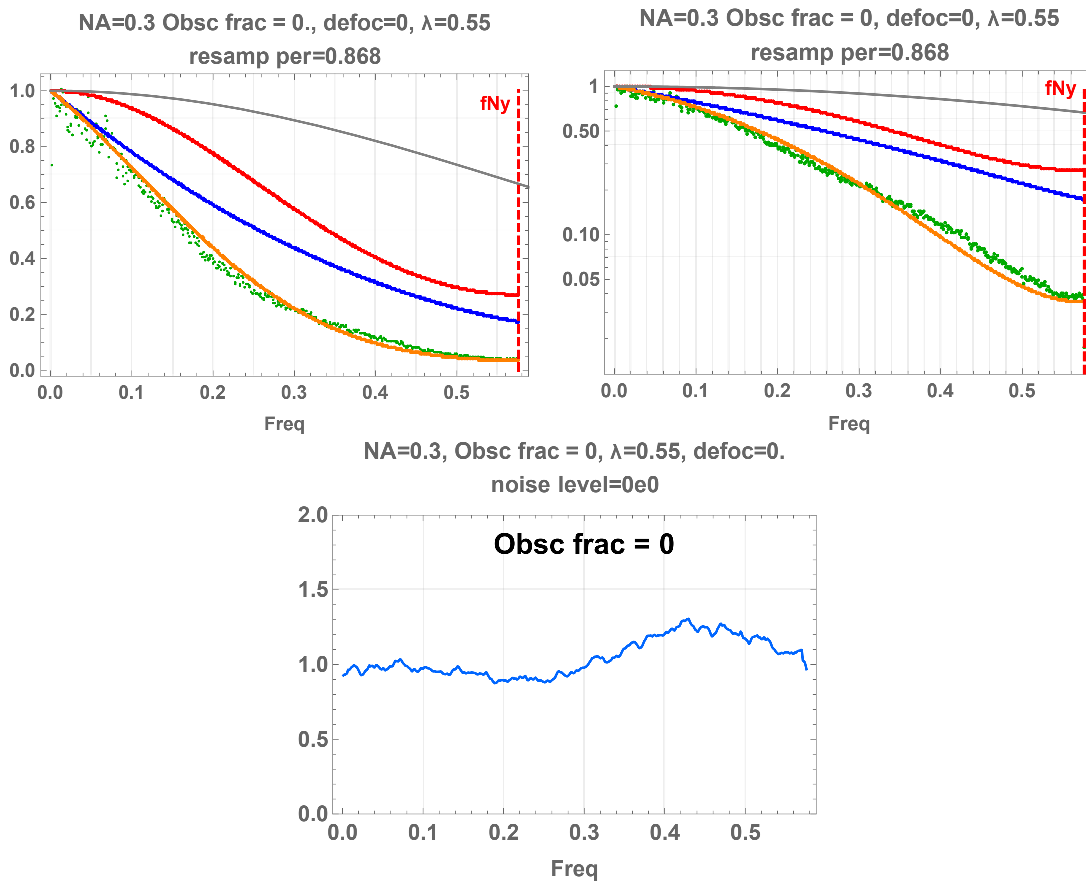

Figure 15 - 10x1x objective model and measured PSDs (upper) with the ratio of measured to model (lower).

The model curve follows the measured PSD up to the middle of the frequency range where the model clearly drops below the measured PSD. This is unlike the other cases above where the model is always greater than the measured PSD at high frequencies. This seems to indicate that the model is underestimating the amount of the aliased signal that is folded back into the sub-Nyquist region.

5. CONCLUSIONS

The simple model of the 1D BPRG has allowed us to investigate practical issues involved in using a BPRA artifact to characterize the ITF of an interferometric microscope. The simple model shows that the expected PSD of an undersampled artifact can be described, not a horizontal line, but by a cosine function with A and B coefficients in the ratio of 2 to 1. More work is needed to refine this model to incorporate the averaging effects of the larger resampled pixels versus the underlying BPRA ground rule size. To be useful as a calibration artifact, the resampled pixel size needs to be such that the Nyquist frequency of the sampling interval lies beyond the cutoff frequency of the lens. This insures that no high frequencies will be aliased back into the measured profile. If the lens cutoff frequency is beyond the Nyquist, then aliasing must be considered, and untangling the ITF from the measured PSD becomes more complicated. Tables 1 and 2 indicate which BPRA patterns would be most useful for calibrating a particular lens-zoom combination. The simple ITF model used in the present work that depends only upon the lens MTF and the pixel sampling MTF indicates that there are additional factors that are not accounted for in the model. More work is needed to identify and model these factors.

ACKNOWLEDGEMENTS

The authors are grateful to Alexander Givental, Ulf Griesmann, and Alan Roginsky for fruitful discussions. This work was partially supported by the U.S. Department of Energy Office of Science, Office of Basic Energy Sciences, and Small Business Technology Transfer (STTR) programs under Award Numbers DE-SC0011352, DE-SC0011352, and DE-SC0011352 to HighRI Optics, Inc. and Rochester Scientific, LLC. Research at the Advanced Light Source and the Molecular Foundry at Lawrence Berkeley National Laboratory is supported by the Office of Science, Office of Basic Energy Sciences, and Material Science Division of the U.S. Department of Energy under Contract No. DE-AC02-05CH11231.

DISCLAIMER

This document was prepared as an account of work sponsored by the United States Government. While this document is believed to contain correct information, neither the United States Government nor any agency thereof, nor The Regents of the University of California, nor any of their employees, makes any warranty, express or implied, or assumes any legal responsibility for the accuracy, completeness, or usefulness of any information, apparatus, product, or process disclosed, or represents that its use would not infringe privately owned rights. Reference herein to any specific commercial product, process, or service by its trade name, trademark, manufacturer, or otherwise, does not necessarily constitute or imply its endorsement, recommendation, or favor by the United States Government or any agency thereof, or The Regents of the University of California. The views and opinions of authors expressed herein do not necessarily state or reflect those of the United States Government or any agency thereof or The Regents of the University of California.

REFERENCES

[1] E. L. Church, and P. Z. Takacs, "Survey of the finish characteristics of machined optical surfaces," Opt. Eng., 24(3), 396-403 (1985).

[2] E. L. Church, and P. Z. Takacs, "Use of an optical-profiling instrument for the measurement of the figure and finish of optical-quality surfaces," Wear, 109, 241-257 (1986).

[3] R. Leach (ed.), [Optical measurement of surface topography], Springer, Berlin Heidelberg, Germany (2011)

[4] S. O. Rice, “Reflection of Electromagnetic Waves from Slightly Rough Surfaces,” Commun. Pure Appl. Math., 4, 361-378 (1951).
[5] P. Beckmann, and A. Spizzichino, [*The Scattering of Electromagnetic Waves from Rough Surfaces*], Pergamon Press, New York, NY (1963)
[6] E. L. Church, and J. M. Zavada, “Residual Surface-Roughness of Diamond-Turned Optics,” Applied Optics, 14(8), 1788-1795 (1975).
[7] E. L. Church, H. A. Jenkinson, and J. M. Zavada, “Measurement of Finish of Diamond-Turned Metal-Surfaces by Differential Light-Scattering,” Optical Engineering, 16(4), 360-374 (1977).
[8] E. L. Church, “The Measurement of Surface Texture and Topography by Differential Light Scattering,” Wear, 57, 93-105 (1979).
[9] E. L. Church, H. A. Jenkinson, and J. M. Zavada, “Relationship between Surface Scattering and Microtopographic Features,” Optical Engineering, 18(2), 125-136 (1979).
[10] E. L. Church, M. R. Howells, and T. V. Vorburger, "Spectral analysis of the finish of diamond-turned mirror surfaces", in Reflecting Optics for Synchrotron Radiation, *Proc. SPIE* **315** (1981), 202-218.
[11] J. M. Bennett, and J. H. Dancy, “Stylus profiling instrument for measuring statistical properties of smooth optical surfaces,” Applied Optics, 20, 1785-1802 (1981).
[12] J. M. Bennett, and L. Mattsson, [*Introduction to Surface Roughness and Scattering*], Optical Society of America, Washington, D.C. (1989) pp.110
[13] C. L. Koliopoulos, and J. C. Wyant, “Profilometer for Diamond-Turned Optics Using a Phase-Shifting Interferometer,” Journal of the Optical Society of America, 70(12), 1591-1591 (1980).
[14] J. C. Wyant, C. L. Koliopoulos, B. Bhushan *et al.*, “An optical profilometer for surface characterization of magnetic media,” ASLE Transactions, 27(2), 101-113 (1984).
[15] B. Bhushan, J. C. Wyant, and C. L. Koliopoulos, “Measurement of surface topography of magnetic tapes by Mirau interferometry,” Applied Optics, 24(10), 1489-1497 (1985).
[16] J. C. Wyant, C. L. Koliopoulos, B. Bhushan *et al.*, “Development of a 3-Dimensional Noncontact Digital Optical Profiler,” Journal of Tribology-Transactions of the Asme, 108(1), 1-8 (1986).
[17] E. L. Church, "The precision measurement and characterization of surface finish", in *Precision Surface Metrology*, Proc. SPIE **429,** pp**.** 86-95 (1983)
[18] E. L. Church, T. V. Vorburger, and J. C. Wyant, “Direct comparison of mechanical and optical measurements of the finish of precision machined and optical surfaces,” Opt. Eng., 24(3), 388-395 (1985).
[19] P. J. de Groot, and X. Colonna de Lega, “Fourier optics modeling of interference microscopes,” Journal of the Optical Society of America A, 37(9), B1 (2020).
[20] P. J. de Groot, “The instrument transfer function for optical measurements of surface topography,” Journal of Physics: Photonics, 3(2), 024004 (2021).
[21] V. V. Yashchuk, W. R. McKinney, and P. Z. Takacs, "Binary pseudo-random grating as a standard test surface for measurement of modulation transfer function of interferometric microscopes", in Advances in Metrology for X-ray and EUV Optics II, *Proc. SPIE* **6704** (2007).
[22] V. V. Yashchuk, W. R. McKinney, and P. Z. Takacs, “Binary pseudorandom grating standard for calibration of surface profilometers,” Optical Engineering, 47(7), 073602 1-5 (2008).
[23] S. K. Barber, P. Soldate, E. H. Anderson *et al.*, "Binary pseudo-random gratings and arrays for calibration of the modulation transfer function of surface profilometers: recent developments", in Advances in X-Ray/EUV Optics and Components IV, *Proc. SPIE* **7448** (2009), 3-12.
[24] S. K. Barber, P. Soldate, E. H. Anderson *et al.*, “Development of pseudorandom binary arrays for calibration of surface profile metrology tools,” Journal of Vacuum Science & Technology B, 27(6), 3213-3219 (2009).
[25] S. K. Barber, E. H. Anderson, R. Cambie *et al.*, “Stability of modulation transfer function calibration of surface profilometers using binary pseudo-random gratings and arrays with nonideal groove shapes,” Optical Engineering, 49(5), - (2010).
[26] T. Etzion, “Constructions for perfect maps and pseudorandom arrays,” IEEE Transactions on Information Theory, 34(5), 1308-1316 (1988).
[27] D. D. Koleske, and S. J. Sibener, “Generation of pseudorandom sequences for use in cross-correlation modulation,” Rev. Sci. Instrum., 63(8), 3852-3855 (1992).
[28] H. D. Lüke, and B. Axel, “Binary arrays with perfect odd-periodic autocorrelation,” Applied Optics, 36(26), 6612-6619 (1997).

[29] S. K. Barber, E. D. Anderson, R. Cambie *et al.*, “Binary pseudo-random gratings and arrays for calibration of modulation transfer functions of surface profilometers,” Nuclear Instruments & Methods in Physics Research Section a-Accelerators Spectrometers Detectors and Associated Equipment, 616(2-3), 172-182 (2010).

[30] V. V. Yashchuk, E. H. Anderson, S. K. Barber *et al.*, “Calibration of the modulation transfer function of surface profilometers with binary pseudorandom test standards: expanding the application range to Fizeau interferometers and electron microscopes,” Optical Engineering, 50(9), (2011).

[31] V. V. Yashchuk, R. Conley, E. H. Anderson *et al.*, “Characterization of electron microscopes with binary pseudo-random multilayer test samples,” Nuclear Instruments & Methods in Physics Research Section a-Accelerators Spectrometers Detectors and Associated Equipment, 649(1), 150-152 (2011).

[32] V. V. Yashchuk, S. Babin, S. Cabrini *et al.*, "Binary pseudorandom array test standard optimized for characterization of large field-of-view optical interferometers", in Interferometry XX, *Proc. SPIE* **11490** (2020), 30. 10.1117/12.2568309

[33] E. L. Church, and P. Z. Takacs, [BASIC Program for Power Spectrum Estimation] Brookhaven National Laboratory, Informal Report 49035 rev. 5/94, (1993).

[34] S. O. Rice, “Mathematical analysis of random noise,” The Bell System Technical Journal, 23(3), 282-332 (1944).

[35] S. O. Rice, “Mathematical analysis of random noise,” The Bell System Technical Journal, 24(1), 46-156 (1945).

[36] G. D. Boreman, [*Modulation Transfer Function in Optical and Electro-Optical Systems, Second Edition*], SPIE Press, Bellingham, WA (2021) pp.156

[37] ISO, [ISO 15529:2010 -- Optics and photonics — Optical transfer function — Principles of measurement of modulation transfer function (MTF) of sampled imaging systems, 3rd edition] ISO/TC 172/SC 1, Geneva, (2010).

[38] H. H. Hopkins, “The Application of Frequency Response Techniques in Optics,” Proc. Phys. Soc., 79, 889-919 (1962).

[39] E. L. O'Neill, “Errata,” J. Opt. Soc. Am., 46, 1096 (1956).

[40] E. L. O''Neill, “Transfer Function for an Annular Aperture,” J. Opt. Soc. Am., 46(4), 283-288 (1956).

[41] A. N. Simonov, and M. C. Rombach, “Asymptotic behavior of the spatial frequency response of an optical system with defocus and spherical aberration,” J. Opt. Soc. Am. A, 27(12), 2563-2573 (2010).

[42] V. V. Yashchuk, K. Munechika, S. Rochester *et al.*, "Reliability investigation of the instrument transfer function calibration technique based on binary pseudo-random array standards", in SPIE Optics and Photonics 2022, Conference OP220: Advances in Metrology for X-Ray and EUV Optics X, (San Diego, August 21-25, 2022); this conference, *Proc. SPIE* (2022).